


Cite this: *RSC Adv.*, 2025, 15, 10622

# Unraveling PPAR $\beta/\delta$ nuclear receptor agonists via a drug-repurposing approach: HTVS-based ligand identification, molecular dynamics, pharmacokinetics, and *in vitro* anti-steatotic validation

Sumit Kumar Mandal,<sup>†a</sup> Mohammed Muzaffar-Ur-Rehman,<sup>†b</sup> Sonakshi Puri,<sup>a</sup> Banoth Karan Kumar,<sup>b</sup> Pankaj Kumar Sharma,<sup>a</sup> Murugesan Sankaranarayanan<sup>b</sup> and P. R. Deepa<sup>\*,a</sup>

Peroxisome proliferator-activated receptors (PPARs) are ligand-activated nuclear receptors with a crucial regulatory role in carbohydrate and lipid metabolism and are emerging druggable targets in "metabolic syndrome" (MetS) and cancers. However, there is a need to identify ligands that can activate specific PPAR subtypes, particularly PPAR $\beta/\delta$ , which is less studied compared with other PPAR isoforms ( $\alpha$  and  $\gamma$ ). Herein, using the drug-repurposing approach, the ZINC database of clinically approved drugs was screened to target the PPAR $\beta/\delta$  receptor through high-throughput-virtual-screening, followed by molecular docking and molecular dynamics (MD) simulation. The top-scoring ligands were subjected to drug-likeness analysis. The hit molecule was tested in an *in vitro* model of NAFLD (non-alcoholic fatty liver disease). The top five ligands with strong binding affinity towards PPAR $\beta/\delta$  were canagliflozin > empagliflozin > lumacaftor > eprosartan > dapagliflozin. RMSD/RMSF analysis demonstrated stable protein–ligand complexation (PLC) by the top-scoring ligands with PPAR $\beta/\delta$ . *In silico* ADMET prediction analysis revealed favorable pharmacokinetic profiles of these top five ligands. Canagliflozin showed significant ( $P < 0.001$ ) dose-dependent decrease in lipid accumulation and the associated oxidative stress-inflammatory response, suggesting its promising anti-steatotic potential. These outcomes pave the way for further validation and development of PPAR activity-modulating therapeutics.

Received 28th December 2024  
Accepted 7th March 2025

DOI: 10.1039/d4ra09055a

rsc.li/rsc-advances

## Introduction

Peroxisome proliferator-activated receptors (PPARs) are a type of nuclear receptors that regulate target gene expression upon binding with ligands.<sup>1</sup> They are subdivided into three isoforms, namely, PPAR $\alpha$ , PPAR $\beta/\delta$  and PPAR $\gamma$ , based on their diverse functions and differential expressions in various tissues and cell types, including the heart, fat tissue, liver and skeletal muscles.<sup>2</sup>

The activation mechanism is quite similar among the three PPAR isoforms, yet they show some differences. For example, PPAR $\alpha$  is activated by fatty acids, while PPAR $\gamma$  is activated by

thiazolidinedione drugs and is reported to be regulated by a natural product, chelerythrine, resulting in an anti-diabetic effect.<sup>3,4</sup> PPAR $\beta/\delta$ , alternatively, has broad ligand specificity, including for fatty acids, eicosanoids, and ligands such as leukotriene B4 and prostacyclin.<sup>5</sup> When these ligands bind to PPARs' ligand binding domain, a conformational change is induced, enabling the PPARs to interact with co-activators and co-repressors. Once activated, the PPARs bind to specific DNA sequences, known as PPAR response elements (PPREs), within the promotor region of the target gene, resulting in the trans-activation of the gene.<sup>6</sup> Transrepression is another PPAR mechanism that occurs without a ligand and is involved in the anti-inflammatory effects of PPARs.<sup>7</sup>

The multi-faceted regulation of lipid metabolism and associated energy mechanisms that have been reported<sup>2,8</sup> are compiled in Fig. 1. It shows that activation of PPAR $\beta/\delta$  inhibits the STAT3/SOCS3 pathway and improves insulin sensitivity in adipose tissue.<sup>9</sup> A recent study has shown that treatment with leptin increases the expression of FGF21 in visceral adipose tissue by activating PPAR $\beta/\delta$ .<sup>10</sup> GW501516, a PPAR $\beta/\delta$  agonist, lowers triglyceride levels in hepatic tissue by restoring hepatic

<sup>a</sup>Biochemistry and Enzyme Biotechnology Laboratory, Department of Biological Sciences, Birla Institute of Technology and Science Pilani, Pilani Campus, Pilani-333 031, Rajasthan, India. E-mail: p20200425@pilani.bits-pilani.ac.in; pankajsharma@pilani.bits-pilani.ac.in; deepa@pilani.bits-pilani.ac.in

<sup>b</sup>Medicinal Chemistry Research Laboratory, Department of Pharmacy, Birla Institute of Technology and Science Pilani, Pilani Campus, Pilani-333 031, Rajasthan, India. E-mail: p20210457@pilani.bits-pilani.ac.in; p20180042@pilani.bits-pilani.ac.in; murugesan@pilani.bits-pilani.ac.in

<sup>†</sup> Authors contributed equally.



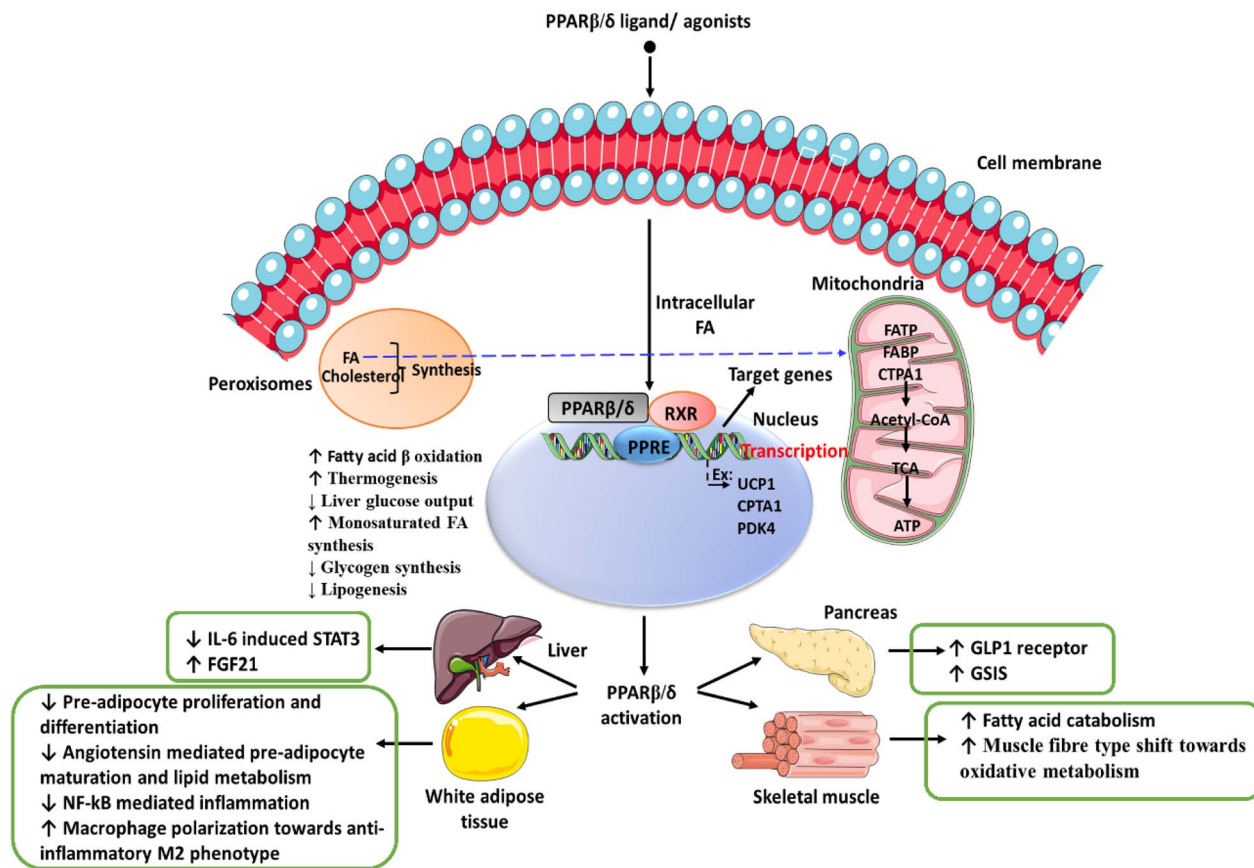


**Fig. 1** The crucial role of PPAR- $\beta/\delta$  in the regulation of lipid metabolism. FA: fatty acids, TCA: tricarboxylic acid, FATP: fatty acid transport protein; FABP: fatty acid binding protein; CPT1A: carnitine palmitoyl transferase I; RXR: retinoid X receptor; ATP: adenosine triphosphate; acetyl-CoA: acetyl coenzyme A; NF- $\kappa$ B: nuclear factor kappa B; IL1, 6, 10: interleukin 1, 6, 10; FGF21: fibroblast growth factor 21; GSIS: glucose-stimulated insulin secretion; GLP-1: glucagon-like peptide 1.

AMPK levels *via* activation of the PGC-1/ $\alpha$ -lipin-1/PPAR $\alpha$  pathway in a rat model.<sup>11,12</sup> Similarly, GW501516 reduces multiple clinical features of metabolic syndrome by increasing the oxidation of fatty acids in skeletal muscles.<sup>13</sup> Metabolic syndrome represents a complement of related disorders that include hyperlipidemia, diabetes mellitus, hypertension, and cardiovascular disorders, which may have the hepatic complication of non-alcoholic fatty liver disease (NAFLD)/non-alcoholic steatohepatitis (NASH).

Studies have also shown that lipolytic functions of PPAR $\beta/\delta$ , which have a potentially beneficial effect on fatty liver disease, are mediated by activating the autophagy pathway and attenuating endoplasmic reticulum stress in obese mice.<sup>14,15</sup> Other beneficial effects reported with respect to PPAR $\beta/\delta$  agonists are mitigation of oxidative stress,<sup>16</sup> inflammation<sup>17,18</sup> and mitochondrial biogenesis,<sup>19</sup> which make it a promising target for identifying PPAR $\beta/\delta$  agonists that could potentially treat metabolic disorders.<sup>20</sup> One of the risks of metabolic syndrome is the development of cancers. In this context, it is important to note that PPAR $\beta/\delta$  has also been evaluated for its potential anti-cancer effects.<sup>16,21–23</sup>

Recently, using a machine learning approach, newer PPAR $\beta/\delta$  agonists were reported.<sup>24</sup> However, there are limited reports

on PPAR $\beta/\delta$  agonists, which prompted the present study. Herein, we screened a database with clinically approved drugs as potential pharmacological candidates using high-throughput virtual screening (HTVS) technique, molecular docking/dynamics simulations and pharmacokinetic profiling. This was followed by biochemical testing of a hit-ligand agonist molecule in an *in vitro* steatotic cell culture model of NAFLD.

## Experimental

### Materials and methods

Computational studies were conducted using the Maestro module within Schrödinger software (v13.3, Schrodinger LLC, NY, USA). Molecular dynamics simulations were carried out utilizing the Desmond module of Schrödinger software, specifically developed by D. E. Shaw (ver. 6.5). Simulations were performed on a Tyrone workstation running on a Linux platform (Ubuntu 22.04 LTS), equipped with 160 GB of RAM and an 11 GB NVIDIA graphics card (GeForce RTX 208 Ti).

HepG2 cells were sourced from the National Centre for Cell Science (NCCS – Pune, India). The minimum essential medium (MEM) was procured from Gibco Life Technologies (Carlsbad, USA), while fetal bovine serum (FBS), oleic acid, and Oil Red O



(ORO) powder were obtained from HiMedia (Mumbai, India). All other chemicals were purchased from Sigma-Aldrich (Schnelldorf, Germany) and were of the highest analytical grade.

### Protein preparation

The protein structures of PPAR $\beta/\delta$  (PDB ID: 3GZ9) were retrieved from the RCSB protein databank (PDB). This protein crystal structure includes a co-crystal ligand, which is reported to be a full agonist of PPAR $\beta/\delta$  and partial agonist of PPAR $\gamma$ .<sup>25,26</sup>

Prior to docking, proteins must be prepared since their crystal structures might have issues including improper bonding orders, missing side chains, loops, and atoms. The Protein Preparation Wizard was used to create the crystal structure of the two proteins, and the purpose of this process was to examine the protein structures and confirm the assignment of bonds and binding orders, the insertion of hydrogens, the identification of disulfide bonds, the completion of any missing loops or side chains, and the rectification of any incorrectly labelled components. Moreover, the OPLS-2005 force field was used to minimize crystal protein structures. Heavy atoms in the structures were constrained to relieve torsional tension using a harmonic potential of 25 kcal mol<sup>-1</sup> throughout the procedure, whereas hydrogen was left unconstrained.<sup>27</sup>

### Ligand preparation

The ligand library of US FDA approved drugs was obtained in SDF format from the approved drug library ZINC database, which comprises 1615 drugs. The ligands were prepared using the LigPrep module of the Schrodinger program for computational studies. Desalting was performed using Epik v4.7, which is based on Hammett and Taft approaches, to achieve the biologically appropriate pH 7 after charge neutralization. PROPKA was used to modify the protonation states of the polar residues. A maximum of one stereoisomer was produced for each compound. In order to produce a low energy conformer, energy minimization of the compounds was carried out utilizing the OPLS-2005 force field.

### Receptor grid generation

The grid box was generated using the receptor's native ligand pose. The receptor grid was generated using receptor-grid generation wizard of the Maestro module of the software. The docked ligands were similar in size compared with native ligands with respect to the grid box, which was the centroid of the native ligands of protein receptors. Using the OPLS-2005 force field, the protein's atoms were fixed within the default van der Waals scaling factor and partial charge cut-off values of 1 and 0.25. The grid box's dimensions were set to 10 × 10 × 10 Å with the co-crystal co-ordinates ( $x = 34.58$ ,  $y = 70.56$ , and  $z = -2.71$ ) and a grid spacing of 1 Å distance.<sup>28</sup>

### Virtual screening and molecular docking

The molecular docking process for FDA-approved drugs from the ZINC<sup>29</sup> database was conducted using the glide module of

Schrödinger, LLC, located in New York, USA. Initially, the HTVS tool was employed to determine whether the ligands were capable of binding to the active site of PPAR $\beta/\delta$ . The ligands that passed this screening were then subjected to further refinement using the standard precision (SP) mode, followed by the extra precision (XP) mode. The HTVS filter output was used as input for the SP filter, and the ligands that successfully passed the SP filter were subsequently subjected to XP docking. Each screening mode utilizes the same scoring function to minimize false positives, but they differ in terms of speed and accuracy. The docking analyses were visualized using the Maestro module of the software. The docking binding energy was utilized to calculate the docking binding affinity of the compounds towards the active site of PPAR $\beta/\delta$  using the following relationship:

$$\Delta G = -RT \ln K_d.$$

In the equation,  $\Delta G$  represents the changes in docking binding energy,  $T$  represents temperature,  $R$  represents the Boltzmann gas constant ( $R = 1.987 \text{ cal mol}^{-1} \text{ K}^{-1}$ ), and  $K_d$  represents dissociation constant. This equation enables the estimation of binding affinity based on the docking binding energy.<sup>30</sup>

### Validation of the docking protocol

The selected protein structures were re-docked with their co-crystal ligands at their active site using the XP docking mode. The generated conformations were superimposed against the native pose to determine their root mean square deviation (RMSD). A deviation value of  $\leq 2.0$  Å validates the docking methodology can be used for docking of the test ligands.

### MM-GBSA studies

Molecular mechanics with generalised Born and surface area solvation (MM-GBSA) is an efficient method to calculate the absolute free energy of a protein–ligand complex.<sup>31</sup> It is the summation of gas-phase energy, solvation energy and entropic contributions. To carry out this study, the docked protein and the ligand's docked conformation were used, and calculations were carried out in the Prime module of Schrodinger software.<sup>32</sup> The solvation model was dielectric surface generalized Born (VSGb) continuum in the presence of the OPLS4 force field.<sup>33</sup>

### Molecular dynamics (MD) simulation studies

The protein–ligand complexes were prepared, optimized, and minimized using the Protein Preparation Wizard of the OPLS 2005 force field. To assess the conformational stability of the protein–ligand complex interactions, a molecular dynamics (MD) simulation was performed using the Desmond module of Schrodinger. The simulation was run for 100 nanoseconds (ns) and employed the OPLS-2005 force field. The protein–ligand complex was placed at the center of an orthorhombic cubic box with dimensions of 10 Å × 10 Å × 10 Å. The simulation included explicit TIP3P water molecules and buffers between the protein



and box edges. In order to neutralize the system, counter ions (such as  $\text{Na}^+$  or  $\text{Cl}^-$ ) were added. Four  $\text{Cl}^-$  ions and 0.15 M NaCl salt concentration were used, and the box volume was minimized using the System Builder wizard in Maestro software.<sup>27,34–36</sup>

The analysis focused on the ligand molecules that showed significant results. The prepared system underwent energy minimization for 100 picoseconds (ps). The final production run consisted of a 100 ns MD simulation conducted under constant temperature and pressure (NPT ensemble) with a relaxation period of 1 ps and a temperature of 300 K. The Nose–Hoover chain coupling technique was used for temperature control. Bonding interactions were calculated with a time step of 2 fs using the reversible reference system propagator algorithm (RESPA) integrator.<sup>37,38</sup> The trajectories obtained from the simulation were examined for the root mean square deviation (RMSD) and root mean square fluctuation (RMSF) of the protein–ligand complex, as well as the RMSF of the ligand itself.

### *In silico* ADMET prediction analysis

After the HTVS and docking of 1615 FDA approved molecules with PPAR $\beta/\delta$ , the pKCSM tool was used to evaluate the ADMET (absorption, distribution, metabolism, elimination, and toxicity) of the top five molecules with the highest docking scores to determine their significant pharmacokinetic features. The ligands with optimal drug-likeness and bioavailability profiles were selected to carry out molecular dynamics studies. The following ADMET parameters were included in the report: absorption: Caco-2 permeability, water solubility, human intestinal absorption, P-glycoprotein substrate, P-glycoprotein I and II inhibitors, and skin permeability; distribution: steady state volume of distribution (VDss), fraction unbound, blood–brain barrier (BBB) permeability, and central nervous system (CNS) permeability; metabolism: cytochrome P450 inhibitors, CYP2D, AMES toxicity, maximum tolerated dosage, hepatotoxicity, and skin sensitization.<sup>39</sup>

Canagliflozin, identified as the top scoring ligand, was experimentally evaluated to evaluate its effectiveness in reducing steatosis in a cell culture model of non-alcoholic fatty liver disease (NAFLD). The subsequent sections detail the experimental confirmation of the pharmacological efficacy of canagliflozin.

### MTT assay for cell viability

HepG2 cells were acquired from the National Centre for Cell Science in Pune, India, and cultured in T-25  $\text{cm}^2$  cell culture flasks. HepG2 cells are a widely accepted and valuable model for studying hepatic steatosis owing to their retention of key hepatocyte functions, including lipid metabolism and accumulation. Furthermore, their established use in steatosis research provides a pool of comparative data, and their ease of culture and reproducibility make them a reliable *in vitro* model.<sup>40</sup> Using this cellular model of NAFLD, we examined the anti-steatotic efficacy of the top-hit ligand, canagliflozin. The cells were maintained at 37 °C with 5%  $\text{CO}_2$  in MEM containing 4.5  $\text{g L}^{-1}$  glucose and 110  $\text{mg L}^{-1}$  sodium pyruvate, supplemented with 10% bovine calf serum (HiMedia). The cell cultures were passaged every 2–3 days,

typically when they reached 80% confluence. Cell viability was assessed by their ability to metabolize the tetrazolium salt MTT (3-(4,5-dimethylthiazol-2-yl)-2,5-diphenyltetrazolium bromide) (SRL Chemicals, Mumbai, India).

To prepare canagliflozin for experiments, it was initially dissolved in dimethyl sulphoxide (DMSO) to prepare a stock solution (SS) with a concentration of 1 mM. Working concentrations of canagliflozin, ranging from 5–100  $\mu\text{M}$ , were then prepared from the stock solution, ensuring that the final concentration of DMSO in the test dilutions did not exceed 1%. Confluent monolayers of HepG2 cells were grown in 96-well plates for 24 hours. These cells were treated with different concentrations of canagliflozin in triplicate and incubated at 37 °C in a  $\text{CO}_2$  environment for 24 hours. After the 24 hour treatment period, the supernatants were aspirated from the wells, and 100  $\mu\text{L}$  of MTT solution (2  $\text{mg mL}^{-1}$ ) was added to each well. The plates were then incubated for 3 hours at 37 °C, followed by the addition of 100  $\mu\text{L}$  DMSO to dissolve the formazan crystals. Optical density was measured at 570 nm using a multi-well spectrophotometer (Multiskan, Thermo Fisher Scientific, Waltham, MA). The safe dose concentration, often considered the concentration at which 80% of cells remain viable, was determined using non-linear regression curve analysis within GraphPad Prism statistical software.<sup>27</sup>

### ORO staining

To test the anti-steatotic effect of the top-agonist canagliflozin (10, 15, and 20  $\mu\text{M}$ ), it was compared with the standard drug saroglitazar (10  $\mu\text{M}$ ).<sup>41</sup> To prepare an ORO solution, 0.5 grams of ORO was diluted in 100 mL of isopropanol to make a stock solution. A working dilution was then prepared by mixing 6 parts of the ORO stock with 4 parts of deionized water. For cell staining, the cells were fixed with 4% paraformaldehyde for 15 minutes at room temperature. After removing paraformaldehyde, the cells were washed with PBS. Subsequently, the freshly prepared ORO working solution was added to the cells, and the cells were kept undisturbed for 15 minutes. The cells were then rinsed with water and immediately examined under a light microscope. To quantify the accumulation of neutral lipids, the stained lipid droplets were dissolved using 100  $\mu\text{L}$  of 100% isopropanol for 5 minutes at room temperature, and the absorbance was measured at 492 nm.<sup>27</sup>

### Lipid peroxidation (LPO) assay

To assess LPO levels, HepG2 cells were seeded in 6 cm plates at a density of  $1 \times 10^5$  cells per well. Subsequently, the cells were exposed to different concentrations of canagliflozin (10, 15, and 20  $\mu\text{M}$ ) and saroglitazar (10  $\mu\text{M}$ ) for 24 hours. Following the treatment, the control and treated cells were collected and sonicated; then, the total protein content was determined using the Bradford method. LPO levels in HepG2 cells were quantified through the thiobarbituric acid-reactive substance (TBARS) assay.

Following treatment, the cells were treated with lysis buffer, homogenized, and centrifuged at  $13\,000 \times g$  for 15 minutes at 4 °C for the lipid peroxidation assay using a modified protocol. The resulting supernatant was collected for subsequent





analysis. The cell lysates from each experimental group were adjusted to contain an equal quantity of protein (1 mg mL<sup>-1</sup>) and were treated with 250  $\mu$ L of 10% trichloroacetic acid (TCA). Afterward, these lysates were mixed with 375  $\mu$ L of 1% (w/v) thiobarbituric acid (TBA) under acidic conditions. This solution was heated in a boiling water bath for 15 minutes, promoting the formation of a pink-colored adduct. The absorbance of this resultant adduct was measured spectrophotometrically at 530 nm using the Multiskan FC (Thermo Scientific, DE). The values obtained were expressed as micromoles ( $\mu$ M) of malondialdehyde per milligram (mg) of protein.<sup>28</sup>

### Statistical analysis

*In vitro* experiments were conducted in a minimum of two to three separate trials, with each trial performed in triplicate sets.

Statistical analysis was carried out using one-way ANOVA to compare the various experimental groups. Significant differences among values were denoted by  $P \leq 0.05$  (\*),  $P \leq 0.01$  (\*\*), and  $P \leq 0.001$  (\*\*\*).

## Results and discussion

### Molecular docking analysis

A total of 1615 compounds were docked into the active site of PPAR $\beta/\delta$ . Using a step-by-step procedure, compounds were primarily screened using HTVS, yielding a top scoring hit, which was then screened using the SP mode. The drugs that failed to bind in the SP mode were excluded, and the remaining drugs were finally docked using an XP mode. The top scoring five ligands were shortlisted, which show the highest affinity towards the PPAR $\beta/\delta$  target protein (Table 1).

**Table 1** Docking scores of the top five ligands at the active sites of PPAR $\beta/\delta$

S. no	Ligands	Drug name	PPAR $\beta/\delta$ (kcal mol <sup>-1</sup> )	MM-GBSA (kcal mol <sup>-1</sup> )
1	ZINC000043207238	Canagliflozin	-13.907	-73.80
2	ZINC000036520252	Empagliflozin	-12.756	-77.09
3	ZINC000064033452	Lumacaftor	-12.509	-58.09
4	ZINC000029319828	Eprosartan	-11.944	-54.77
5	ZINC000003819138	Dapagliflozin	-11.86	-71.22
6	Co-crystal ligand	(2,3-Dimethyl-4-[[2-(prop-2-yn-1-yloxy)-4-[[4-(trifluoromethyl)phenoxy]methyl]phenyl]sulfanyl]phenoxy)acetic acid	-12.74	-96.96

**Table 2** Amino acid interactions of the top-scoring ligands<sup>a</sup>

Ligands	PPAR $\beta/\delta$		
	Residues	Type of interactions	Distance ( $\text{\AA}$ )
ZINC000043207238 (canagliflozin)	THR288	Halogen bond	1.93
	THR289	H-Bond	1.81
	HIS449	Halogen bond	2.00
	HIS449	Halogen bond	2.50
	PHE282	Halogen bond	2.58
	PHE282	Halogen bond	2.12
	PHE282	Halogen bond	2.00
	PHE282	Halogen bond	2.44
ZINC000036520252 (empagliflozin)	THR288	H-Bond	2.12
	THR288	Halogen bond	3.06
	HIS449	Halogen bond	5.71
	LYS367	Halogen bond	6.68
ZINC000064033452 (lumacaftor)	HIS449	H-Bond	1.92
	HIS449	Halogen bond	3.73
ZINC000029319828 (eprosartan)	CYS285	Aromatic H-bond	2.13
	PHE327	Aromatic H-bond	2.43
	THR289	Halogen bond	2.07
ZINC000003819138 (dapagliflozin)	PHE327	Aromatic H-bond	3.64
	THR289	H-Bond	2.74
Co-crystal ligand	THR288	H-Bond	2.00
	TYR473	H-Bond	1.82
	HIS449	H-Bond	1.80
	HIS449	Pi-Pi	4.47
	THR288	H-Bond	2.00

<sup>a</sup> Abbreviations: PPAR $\beta/\delta$  = peroxisome proliferator activated receptor  $\beta/\delta$ ; kcal = kilocalorie; mol = mole.



for the treatment of type 2 diabetes, exhibited significant docking scores against PPAR $\beta/\delta$  ( $-13.907$  kcal mol $^{-1}$ ). When canagliflozin was docked against PPAR $\beta/\delta$ , it formed four



hydrogen bond interactions with Thr288, Thr289, His449 and Phe282. Empagliflozin, a sodium-glucose co-transporter 2 inhibitor used to improve glycemic control in adults with type 2 diabetes mellitus, showed a similar interaction pattern. It formed hydrogen bonds with Thr288 and halogen bonds with Thr288, His449, Lys367. Lumacaftor, used for the treatment of cystic fibrosis, interacted with PPAR  $\beta/\delta$  through hydrogen bonds with His449 and formed one halogen bond with His449. Eprosartan, an angiotensin II receptor inhibitor used for the treatment of high blood pressure, formed two aromatic bond interactions with Cys285 and Phe327. It also exhibited one halogen bond interaction with Thr289. Dapagliflozin, a sodium-

glucose transport protein sub-type 2 inhibitor used in type 2 diabetes treatment, formed hydrogen bonds with Thr289 and one aromatic H-bond with Phe327 (Fig. 2). Overall, the docking interactions and bond distances of the top five drugs with different PPAR $\beta/\delta$  molecules are summarized in Table 2.

### Molecular dynamics simulation studies

Molecular dynamics results of the co-crystal and the hit molecule (ZINC000043207238) have shown a stable RMSD plot. In the case of the co-crystal ligand, the docked complex exhibits three H-bond interactions. One H bond was formed *via*

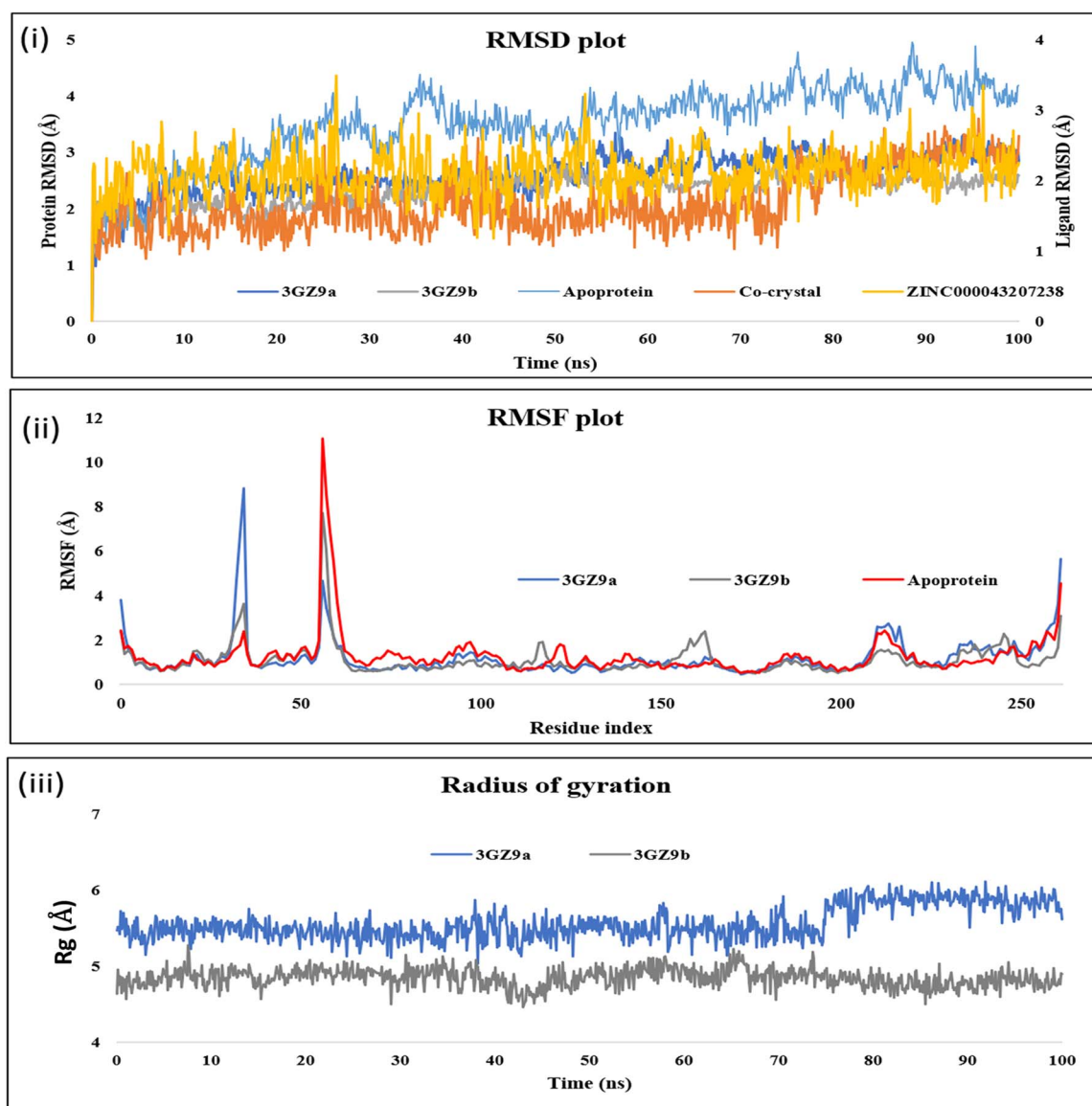


**Fig. 3** (i) RMSD plot depicting the deviation of the protein and ligands during the simulation. 3GZ9a indicates the protein with the hit compound, while 3GZ9b indicates the protein with the co-crystal ligand, orange line indicates the co-crystal ligand, and yellow indicates the hit compound. (ii) RMSF plot depicting fluctuations of the protein residues during simulation. 3GZ9a indicates the protein with respect to the co-crystal ligand and 3GZ9b with respect to the hit compound. (iii) Depiction of the radius of gyration ( $R_g$ ) graph of the top-scoring ligand (canagliflozin) complexed with 3GZ9 and co-crystal ligand complexed with 3GZ9 during 100 ns MD Simulation. 3GZ9a indicates the protein with respect to the co-crystal ligand and 3GZ9b with respect to the hit compound.



interaction of the oxygen atom between the rings A and B with Thr288. The other two interactions were due to interaction of carboxylic terminal with His449 and Tyr473. In the initial stage of the dynamics, the interaction between the ligand and Thr288 disappeared, resulting in an RMSD of 1.2 Å. During the entire simulation, there were very few deviations in the ligand within the range of 2.0 Å (from 1.2 Å to 3.2 Å) (Fig. 3(i)). The residues interacting with the ligand had fewer fluctuations between 0.6 Å and 1.8 Å, as can be seen in the RMSF plot (Fig. 3(ii)), indicating stable protein in the presence of a co-crystal ligand. The major contributing residues in the interactions include His449 (41% H bonds and 40% pi-pi stacking) and Tyr473 (43% H bonds) (Fig. 4(i)).

The radius of gyration ( $R_g$ ), which determines the compactness of the protein, shows very less deviation between 5.1 Å and 6.0 Å (Fig. 3(iii)). In the case of the hit compound, the docked complex had only one H-bond interaction with Gln286 with

a distance of 1.81 Å. After initiating dynamics, the bond between the 5th hydroxy group of glucopyranose of the hit molecule and Gln286 disappeared, and the interaction of His323 with the 3rd hydroxy group was seen, resulting in a change in conformation of the docked ligand, thereby increasing the RMSD to 2.4 Å (Fig. 3). Furthermore, new interactions were observed with Leu339, Val341, Lys367, His449 and Tyr473 until 40 ns. After 55 ns, two additional residues, Gln286 and His323, were observed to form strong interactions. Among these, residues that contributed to direct interactions with the ligand include Gln286, Tyr473, and His449, with 24%, 11%, and 36%, respectively. The residue His323 contributed to water-mediated interactions (11%). In addition, other residues such as Leu339, Val341, and Lys367 formed water-mediated interactions, and their contributions were less than 10% (Fig. 4(ii)). The RMSF plot (Fig. 3(ii)) also shows very low fluctuations of the residues under interaction with the ligand (<2.0 Å). The

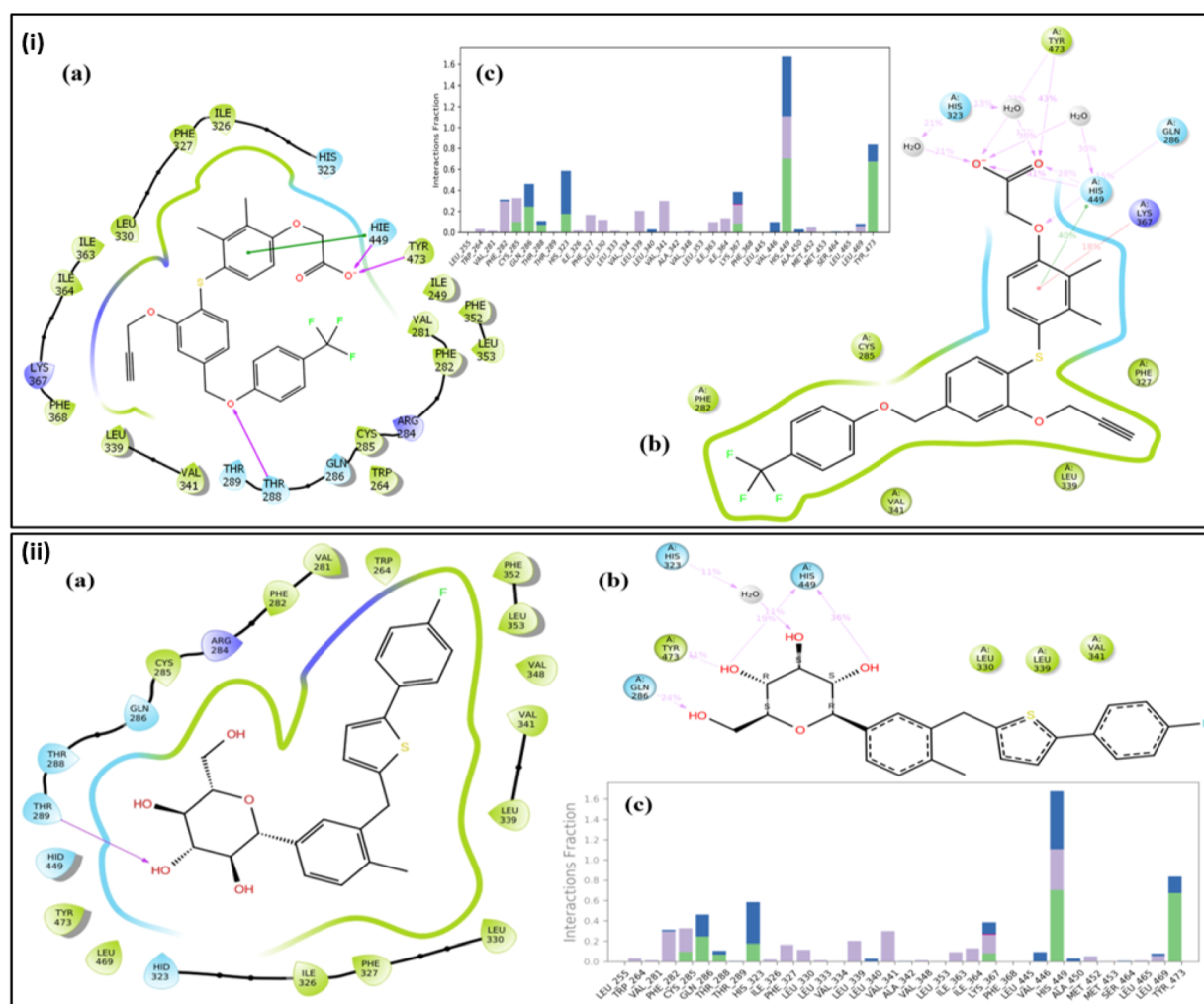


Fig. 4 (i) Analysis of amino acid residue interactions during molecular dynamics simulation. 2D interaction diagram of co-crystal representing the (a) docked pose (b) residual contribution during the simulation and (c) histogram graph and percentage of interaction fraction wherein green indicates an H bond, purple indicates a hydrophobic bond, pink indicates an ionic bond, and blue indicates water bridges. (ii) Analysis of amino acid residue interactions during molecular dynamics simulation. 2D interaction diagram of ZINC000043207238 (canagliflozin) representing the (a) docked pose (b) residual contribution during the simulation, and (c) histogram graph and percentage of interaction fraction, wherein green indicates an H bond, purple indicates a hydrophobic bond, pink indicates an ionic bond, and blue indicates water bridges.



deviations in the  $R_g$  was  $<1.5$  Å (between 4.0–5.25 Å) (Fig. 3(iii)), and the overall deviations in the RMSD plot were not more than 2.0 Å (1.5–3.2 Å). This indicates that the ligand is stable in the active site pocket and is retained within the pocket till the end of the simulation.

For comparison, the PPAR $\beta/\delta$  protein in its apo-form was subjected to dynamics studies for 100 ns. As depicted in Fig. 3(i), the RMSD of the apo-protein has a deviation ranging from 2.0 Å to 5.0 Å, while the protein when complexed with the co-crystal or the hit compound has a lower deviation (2.0–3.0 Å). This indicates that the presence of ligands in the active site of the protein resulted in stability, as evident from the decreased protein deviation or residual fluctuation observed in the respective RMSD and RMSF plots (Fig. 3(i and ii)). We also observed most of the interactions with the co-crystal ligand are due to the acetic acid group, while the hit compound engages *via* hydroxyl groups on its pyranose rings. The co-crystal and the hit compound showed similar behaviour in their dynamics and interaction pattern, which suggested that the hit compound (canagliflozin) could have agonistic behaviour similar to that of the co-crystal ligand, which encouraged us to further carry out *in vitro* investigation.

### *In silico* ADMET prediction and drug-likeness analysis

The top five agonists for the protein target of PPAR $\beta/\delta$  were chosen. All the ligands showed better docking scores against PPAR $\beta/\delta$  protein targets. Further testing was performed on these five ligands for *in silico* drug-likeness prediction and ADMET analysis. These top scored ligands met the requirements for polarity, hydrophobicity, and lipophilicity. This study aids in the selection of the finest molecules with drug-like properties and polarities that are biologically permeable.

Table 3 presents a summary of the predicted ADMET characteristic results for the top five PPAR $\beta/\delta$  agonists. Based on the comparison between the marginal value and the actual value, ADMET results were interpreted as high Caco-2 permeability predicted value  $>0.90$ , intestinal absorption less than 30% is considered to be poorly absorbed, human VDss is low if it is less than  $0.71 \text{ L kg}^{-1}$  and high if it is more than  $2.81 \text{ L kg}^{-1}$ , BBB permeability  $\log \text{BB} >0.3$  is considered to cross BBB, and  $\log \text{BB} 1$  are poorly distributed. Compounds with a  $\log \text{PS}$  of  $>2$  and  $<3$  have the ability to permeate the central nervous system (CNS). The favourable pharmacokinetic profile of the top scoring ligands, as revealed by the above ADMET analysis, is yet another point for considering these ligands as potential PPAR $\beta/\delta$  agonist drug candidates.

The ADMET analysis of canagliflozin in our study is in resonance with other research reports. Studies have shown that canagliflozin is rapidly and completely absorbed from the gastrointestinal tract, with a peak plasma concentration reached within 1–2 hours after oral administration.<sup>42</sup> Food does not significantly affect its absorption. Canagliflozin is highly protein-bound (99%) in the plasma, mainly to albumin. It has a large volume of distribution, indicating that it gets distributed extensively to tissues.<sup>43</sup> Canagliflozin is primarily metabolized in the liver *via* glucuronidation, a phase II metabolic pathway. The

Table 3 *In silico* predicted pharmacokinetic (ADMET) analysis of the top-scoring ligands

Parameters	Absorption			Distribution					Lipinski's rule of five				
	Water solubility ( $\log \text{mol L}^{-1}$ )	Caco2 permeability ( $\log \text{cm s}^{-1}$ )	Intestinal absorption (% human)	Skin permeability ( $\log K_p$ )	P-Glycoprotein substrate	P-Glycoprotein inhibitor	VDss (human) ( $\log \text{L kg}^{-1}$ )	Fraction unbound (human) (Fu)	BBB permeability ( $\log \text{BB}$ )	CNS permeability ( $\log \text{PS}$ )	Molecular weight	Rotatable bonds	log <i>P</i>
Canagliflozin	−4.21	0.85	0.85	−2.7	Yes	Yes	−0.71	0.08	−0.99	−3.02	444.52	5	2.97
Empagliflozin	−3.56	−0.02	55.87	−2.7	Yes	Yes	−0.38	0.07	−1.10	−3.51	450.91	6	1.613
Lumacaftor	−3.18	0.63	78.71	−2.7	Yes	No	−1.46	0.03	−0.47	−2.81	452.41	5	4.75
Eprosertan	−2.89	0.67	57.17	−2.7	Yes	No	−0.72	0.14	−0.87	−2.47	424.52	10	4.74
Dapagliflozin	−3.43	0.94	55.86	−2.7	Yes	Yes	−0.33	0.08	−0.99	−3.34	408.88	6	1.84
Parameters	Metabolism			Excretion			Toxicity			Donors			
	CYP substrate	CYP inhibitors	Total clearance ( $\log \text{mL min}^{-1} \text{kg}^{-1}$ )	Renal OCT2 substrate	AMES toxicity	Hepatotoxicity	Skin sensitization	Molecular weight	log <i>P</i>	Rotatable bonds	Acceptors	Donors	Surface area
Canagliflozin	No	No	0.035	No	No	No	No	444.52	2.97	5	6	4	183.56
Empagliflozin	No	No	0.40	No	No	No	No	450.91	1.613	6	7	4	185.31
Lumacaftor	No	No	−0.10	No	No	Yes	No	452.41	4.75	5	5	2	186.53
Eprosertan	No	No	0.67	No	No	Yes	No	424.52	4.74	10	5	2	178.70
Dapagliflozin	No	No	0.19	No	No	No	No	408.88	1.84	6	6	4	168.47



major enzymes involved are UGT1A9 and UGT2B4, whereas CYP3A4, a phase I enzyme, plays a minor role in its metabolism.<sup>44</sup> Canagliflozin is mainly excreted in the feces (about 50%) as an unchanged drug and metabolite. About 33% is excreted in the urine as metabolites. The terminal half-life of canagliflozin is about 10–13 hours.<sup>45</sup> Overall, the outcomes of ADMET analysis of canagliflozin in the present study and from other reports indicate that it has favorable pharmacokinetic properties, which contribute to its efficacy and safety profile in the treatment of type 2 diabetes and potentially other metabolic disorders.

### Canagliflozin suppresses intracellular lipid accumulation in HepG2 cells

Before assessing the anti-steatotic impact of canagliflozin, we determined its safe dosage by examining its dose-dependent effects on HepG2 cell viability using the MTT assay. Subsequently, we employed non-cytotoxic doses of canagliflozin (10, 15, and 20  $\mu\text{M}$ ) for further *in vitro* investigations (Fig. 5a).

To induce cellular lipid deposits in HepG2 hepatocytes, we supplemented them with free fatty acids (oleic acid) for 48

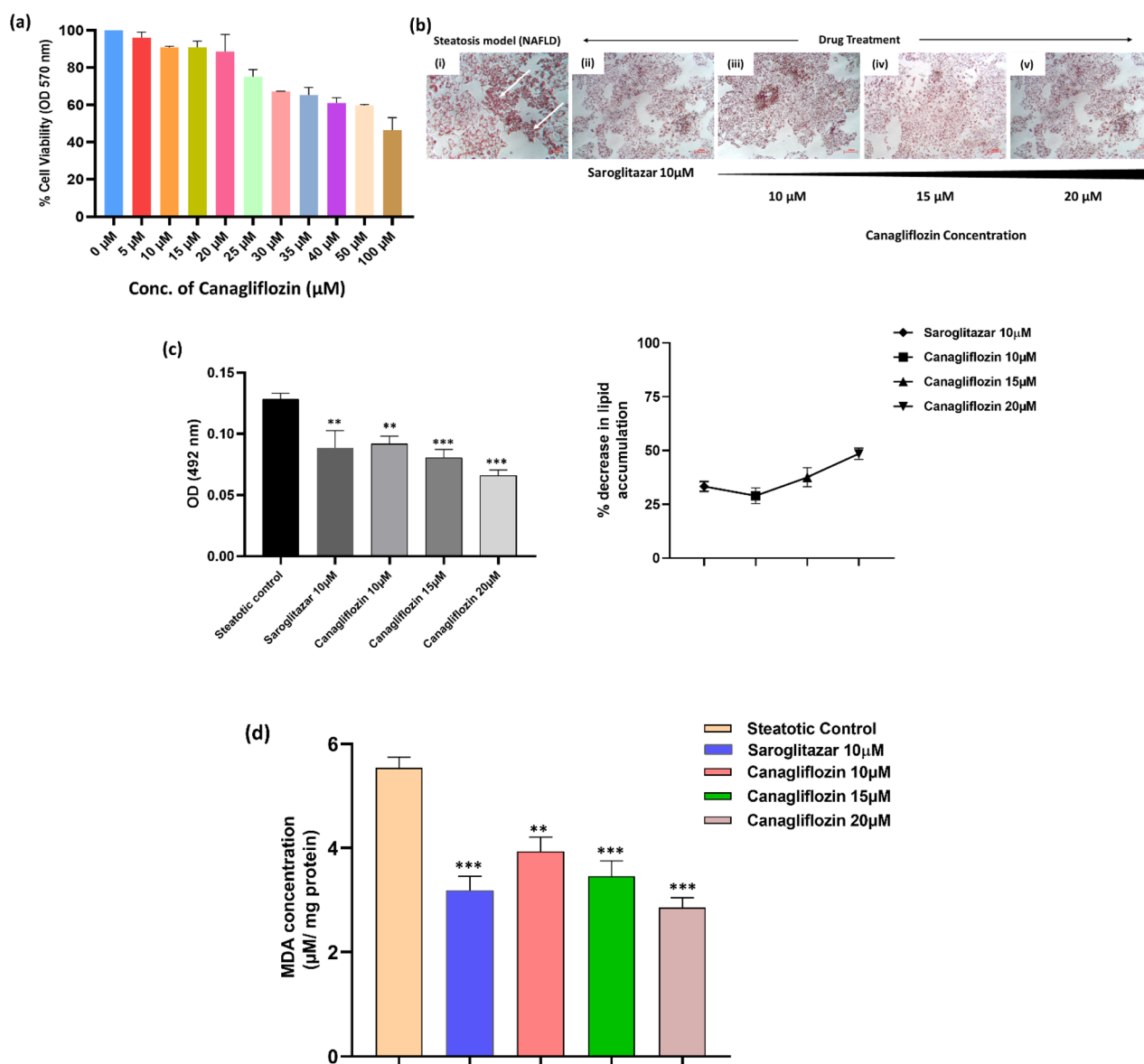


**Fig. 5** Inhibitory effects of canagliflozin on lipid accumulation in the *in vitro* model of NAFLD. (a) Canagliflozin's inhibitory effects on lipid accumulation in an *in vitro* model of NAFLD were evaluated by assessing dosage-dependent impacts on HepG2 cells after 24 hours of treatment using the MTT assay. Results are presented as the mean  $\pm$  S.D. of a minimum of three experiments conducted in triplicate. (b) Photomicrographs at 10 $\times$  magnification illustrated intense Oil Red O (ORO) staining in the untreated steatotic NAFLD group (i), contrasted by reduced lipid staining in the canagliflozin-treated groups (ii–v). White arrows indicate lipid accumulation stained with ORO. (c) Quantification of ORO staining revealed a dose-dependent inhibition of lipid accumulation (steatosis). Values are expressed as the mean  $\pm$  S.D. of a minimum of three experiments. (d) The reduction in malondialdehyde (MDA) levels in the treated groups confirmed the anti-NAFLD protection conferred by canagliflozin. Values are expressed as the mean  $\pm$  S.D. of a minimum of three experiments conducted in triplicate. Symbols \*, \*\*, and \*\*\* denote statistical significance at  $P \leq 0.05$ , 0.01, and 0.001, respectively.

hours. Canagliflozin, identified as the top hit, demonstrated a concentration-dependent reduction in lipid accumulation in steatotic cells following a 24 hour treatment, which was evaluated using ORO staining (Fig. 5a and b). This anti-steatotic effect was comparable to that observed with the positive control saroglitazar (10  $\mu$ M). Specifically, neutral lipids such as triglycerides, stained with ORO, were quantified spectrophotometrically at 492 nm. Fig. 5c illustrates a consistent reduction in triglyceride (TG) accumulation as the concentration of canagliflozin increased ( $p < 0.05$ ). The doses of 10, 15, and 20  $\mu$ M resulted in lipid accumulation reductions in the steatotic cells by 29.03%, 37.57%, and 48.45%, respectively, while saroglitazar, the reference anti-steatotic drug control, induced a 33.39% reduction.

Lipotoxicity induced by steatosis resulted in oxidative stress in the hepatocytes, evident from an increase in malondialdehyde levels in the disease (control) group (Fig. 5d). This oxidative stress-induced lipid peroxidation was attenuated in the cells treated with canagliflozin. In this study, we observed a reduction in lipid peroxidation by 27.99%, 33.50%, and 46.10% when treated with 10, 15, and 20  $\mu$ M of canagliflozin, respectively. This is similar to the oxidative reduction observed when cells were treated with the reference drug saroglitazar at 10  $\mu$ M.

## Conclusion

Using a high throughput virtual screening and molecular docking approach, a list of top-scoring ligands with potential as PPAR $\beta/\delta$  receptor-agonists were identified in this study. These ligands can be experimentally validated in metabolic syndrome and cancers, where the nuclear receptor PPAR $\beta/\delta$  plays a significant mechanistic role. The top-hit molecule (canagliflozin), in the present study, showed favourable protein–ligand complex stability, pharmacokinetic properties, and pharmacological efficacy in controlling hepatic fat accumulation and associated oxidative stress in NAFLD/NASH.

## Abbreviations

PPAR	Peroxisome proliferator-activated receptors
PPREs	Peroxisome proliferator-activated receptor response elements
FDA	Food and drug administration
RXR	Retinoid X receptor
NAFLD	Non-alcoholic fatty liver disease
NASH	Non-alcoholic steatohepatitis
HTVS	High throughput virtual screening
MD	Molecular dynamics
PDB	Protein Data Bank
OPLS-2005	Optimized potentials for liquid simulations 2005
SP	Standard precision
XP	Extra precision
RMSD	Root mean square deviation
RMSF	Root mean square fluctuation

$R_g$	Radius of gyration
MM-GBSA	Molecular mechanics with generalised Born and surface area solvation
RESPA	Reversible reference system propagator algorithms
VSGB	Variable dielectric generalized Born

## Data availability

The original contributions presented in the study are included in the article. Further inquiries can be directed to the corresponding author.

## Author contributions

P. R. Deepa (PRD), Sankaranarayanan Murugesan (SM): Conceptualization; Sumit Kumar Mandal (SKM), Mohammed Muzaffar-Ur-Rehman (MMR), Sonakshi Puri (SP), Banoth Karan Kumar (BKK): methodology & experimentation; SKM, SP, BKK, MMR: data curation, software; SKM, SP, MMR, & BKK: writing and original draft preparation; SKM, SP, BKK, MMR, SM: software and data validation; PRD, SM, PKS: visualization, investigation, supervision; SKM, SP, MMR, PRD, SM, PKS: writing – reviewing and editing.

## Conflicts of interest

The authors declare that they have no conflict of interest.

## Acknowledgements

The research grant from the Indian Council of Medical Research (52/13/2022-BIO/BMS), Govt. of India, New Delhi, is acknowledged. SKM, SP and MMR acknowledged the Institute Fellowship from BITS Pilani, and BKK is grateful to the Ministry of Tribal Affairs, Government of India, for the research fellowship. SM acknowledges the research support from the Department of Biotechnology (Indo-Spain Bilateral Programme), Govt. of India, New Delhi.

## References

- 1 J. N. Feige, L. Gelman, L. Michalik, B. Desvergne and W. Wahli, *Prog. Lipid Res.*, 2006, **45**, 120–159.
- 2 B. Grygiel-Górniak, *Nutr. J.*, 2014, **13**, 1–10.
- 3 V. M. W. Gee, F. S. L. Wong, L. Ramachandran, G. Sethi, A. P. Kumar and C. W. Yap, *J. Comput.-Aided Mol. Des.*, 2014, **28**, 1143–1151.
- 4 W. Zheng, L. Qiu, R. Wang, X. Feng, Y. Han, Y. Zhu, D. Chen, Y. Liu, L. Jin and Y. Li, *Sci. Rep.*, 2015, **5**, 12222.
- 5 L. Han, W. J. Shen, S. Bittner, F. B. Kraemer and S. Azhar, *Future Cardiol.*, 2017, **13**, 279–296.
- 6 S. Tyagi, P. Gupta, A. Saini, C. Kaushal and S. Sharma, *J. Adv. Pharm. Technol. Res.*, 2011, **2**, 236–240.
- 7 A. Fougerat, A. Montagner, N. Loiseau, H. Guillou and W. Wahli, *Cells*, 2020, **9**, 1638.
- 8 J.-C. Fruchart, B. Staels and P. Duriez, *Curr. Atheroscler. Rep.*, 2001, **3**, 83–92.



- 9 L. Serrano-Marco, R. Rodríguez-Calvo, I. El Kochairi, X. Palomer, L. Michalik, W. Wahli and M. Vázquez-Carrera, *Diabetes*, 2011, **60**, 1990–1999.
- 10 L. Mazuecos, C. Pintado, B. Rubio, E. Guisantes-Batán, A. Andrés and N. Gallardo, *Int. J. Mol. Sci.*, 2021, **22**(9), 4624.
- 11 E. Barroso, R. Rodríguez-Calvo, L. Serrano-Marco, A. M. Astudillo, J. Balsinde, X. Palomer and M. Vázquez-Carrera, *Endocrinology*, 2011, **152**, 1848–1859.
- 12 S. Li, Y. Zhi, W. Mu, M. Li and G. Lv, *Eur. J. Pharmacol.*, 2023, 176300.
- 13 D. Sprecher, T. Johnson, E. Olson, S. Hirschberg, A. Liu, Z. Fang, P. Hegde, D. Richards, L. Sarov-blatt, J. C. Strum, S. Basu, J. Cheeseman, B. A. Fielding, S. M. Humphreys, T. Danoff, N. R. Moore, P. Murgatroyd, S. O. Rahilly, P. Sutton, T. Willson, D. Hassall, K. N. Frayn and F. Karpe, *Diabetes*, 2008, **57**(2), 332–339.
- 14 L. Tong, L. Wang, S. Yao, L. Jin, J. Yang, Y. Zhang, G. Ning and Z. Zhang, *Cell Death Dis.*, 2022, **15**, 113127.
- 15 F. M. Silva-Veiga, T. L. Rachid, L. de Oliveira, F. Graus-Nunes, C. A. Mandarim-de-Lacerda and V. Souza-Mello, *Mol. Cell. Endocrinol.*, 2018, **474**, 227–237.
- 16 S. Du, N. Wagner and K. Wagner, *PPAR Res.*, 2020, **2020**(1), 3608315.
- 17 Y. Tobita, T. Arima, Y. Nakano, M. Uchiyama, A. Shimizu and H. Takahashi, *Int. J. Mol. Sci.*, 2020, **21**, 1–13.
- 18 W. Shan, P. S. Palkar, I. A. Murray, E. I. Mcdevitt, M. J. Kennett, B. H. Kang, H. C. Isom, G. H. Perdew, F. J. Gonzalez and J. M. Peters, *Toxicol. Sci.*, 2008, **105**, 418–428.
- 19 M. Webb, D. P. Sideris and M. Biddle, *Bioorg. Med. Chem. Lett.*, 2019, **29**, 1270–1277.
- 20 L. Xiao and N. Wang, *J. Mol. Cell. Cardiol.*, 2022, **169**, 1–9.
- 21 X. Wang, G. Wang, Y. Shi, L. Sun, R. Gorczynski, Y.-J. Li, Z. Xu and D. E. Spaner, *Oncogenesis*, 2016, **5**, e232.
- 22 T. T. L. Wu, H. S. Niu, L. J. Chen, J. T. Cheng and Y. C. Tong, *Eur. J. Pharmacol.*, 2016, **775**, 35–42.
- 23 N. Wagner and K. D. Wagner, *Cells*, 2022, **11**(15), 2432.
- 24 B. Da'adoosh, D. Marcus, A. Rayan, F. King, J. Che and A. Goldblum, *Sci. Rep.*, 2019, **9**, 1106.
- 25 R. V Connors, Z. Wang, M. Harrison, A. Zhang, M. Wanska, S. Hiscock, B. Fox, M. Dore, M. Labelle and A. Sudom, *Bioorg. Med. Chem. Lett.*, 2009, **19**, 3550–3554.
- 26 H. M. Berman, J. Westbrook, Z. Feng, G. Gilliland, T. N. Bhat, H. Weissig, I. N. Shindyalov and P. E. Bourne, *Nucleic Acids Res.*, 2000, **28**, 235–242.
- 27 S. K. Mandal, B. K. Kumar, P. K. Sharma, S. Murugesan and P. R. Deepa, *Comput. Biol. Med.*, 2022, **147**, 105796.
- 28 S. K. Mandal, S. Puri, B. K. Kumar, M. Muzaffar-Ur-Rehman, P. K. Sharma, M. Sankaranarayanan and P. R. Deepa, *Mol. Diversity*, 2024, **28**, 1423–1438.
- 29 D. E. Shaw, J. P. Grossman, J. A. Bank, B. Batson, J. A. Butts, J. C. Chao, M. M. Deneroff, R. O. Dror, A. Even, C. H. Fenton, A. Forte, J. Gagliardo, G. Gill, B. Greskamp, C. R. Ho, D. J. Ierardi, L. Iserovich, J. S. Kuskin, R. H. Larson, T. Layman, L. S. Lee, A. K. Lerer, C. Li, D. Killebrew, K. M. Mackenzie, S. Y. H. Mok, M. A. Moraes, R. Mueller, L. J. Nociolo, J. L. Peticolas, T. Quan, D. Ramot, J. K. Salmon, D. P. Scarpazza, U. Ben Schafer, N. Siddique, C. W. Snyder, J. Spengler, P. T. P. Tang, M. Theobald, H. Toma, B. Towles, B. Vitale, S. C. Wang and C. Young, in *International Conference for High Performance Computing, Networking, Storage and Analysis, SC*, IEEE, 2014, vol. 2015, pp. 41–53.
- 30 W. L. Jorgensen, D. S. Maxwell and J. Tirado-Rives, *J. Am. Chem. Soc.*, 1996, **118**, 11225–11236.
- 31 S. Genheden, O. Kuhn, P. Mikulskis, D. Hoffmann and U. Ryde, *J. Chem. Inf. Model.*, 2012, **52**, 2079–2088.
- 32 C. Mulakala and V. N. Viswanadhan, *J. Mol. Graphics Modell.*, 2013, **46**, 41–51.
- 33 Y. Sixto-López, M. Bello and J. Correa-Basurto, *J. Comput.-Aided Mol. Des.*, 2020, **34**, 857–878.
- 34 K. J. Bowers, E. Chow, H. Xu, R. O. Dror, M. P. Eastwood, B. A. Gregersen, J. L. Klepeis, I. Kolossvary, M. A. Moraes, F. D. Sacerdoti, J. K. Salmon, Y. Shan and D. E. Shaw, in *Proceedings of the 2006 ACM/IEEE Conference on Supercomputing*, SC'06, 2006, pp. 84.
- 35 M. P. Jacobson, R. A. Friesner, Z. Xiang and B. Honig, *J. Mol. Biol.*, 2002, **320**, 597–608.
- 36 V. Kumar, J. K. Dhanjal, S. C. Kaul, R. Wadhwa and D. Sundar, *J. Biomol. Struct. Dyn.*, 2020, **39**, 1–13.
- 37 M. Ikeguchi, *J. Comput. Chem.*, 2004, **25**, 529–541.
- 38 S. J. Stuart, R. Zhou and B. J. Berne, *J. Chem. Phys.*, 1996, **105**, 1426–1436.
- 39 D. E. V. Pires, T. L. Blundell and D. B. Ascher, *J. Med. Chem.*, 2015, **58**, 4066–4072.
- 40 F. A. Müller and S. J. Sturla, *Curr. Opin. Toxicol.*, 2019, **16**, 9–16.
- 41 M. R. Jain, S. R. Giri, B. Bhoi, C. Trivedi, A. Rath, R. Rathod, R. Ranvir, S. Kadam, H. Patel and P. Swain, *Liver Int.*, 2018, **38**, 1084–1094.
- 42 D. Devineni and D. Polidori, *Clin. Pharmacokinet.*, 2015, **54**, 1027–1041.
- 43 E. Hoebe, W. De Winter, M. Neyens, D. Devineni, A. Vermeulen and A. Dunne, *Clin. Pharmacokinet.*, 2016, **55**, 209–223.
- 44 P. Kaur, B. S. Behera, S. Singh and A. Munshi, *Eur. J. Pharmacol.*, 2021, **904**, 174169.
- 45 D. Devineni, J. Murphy, S. Wang, H. Stieltjes, P. Rothenberg, E. Scheers and R. N. V. S. Mamidi, *Clin. Pharmacol. Drug Dev.*, 2015, **4**, 295–304.

